


## Phase field modeling in liquid binary mixtures: Isothermal and nonisothermal problems

Rodica Borcia <sup>\*</sup>, Ion Dan Borcia , and Michael Bestehorn

*Institut für Physik, Brandenburgische Technische Universität Cottbus–Senftenberg,  
Cottbus D-03044, Germany*

Deewakar Sharma and Sakir Amiroudine 

*Université Bordeaux, I2M UMR Centre National de la Recherche Scientifique 5295, Talence F-33400, France*



(Received 14 December 2021; accepted 23 May 2022; published 13 June 2022;  
corrected 9 November 2022)

Based on the conservative phase field model developed by Lowengrub and Truskinovsky [Proc. R. Soc. London A **454**, 2617 (1998)] for almost incompressible liquid binary mixtures, we propose an extended scheme for studying immiscible/miscible liquids. Below a critical temperature  $T_c$ , the liquids are immiscible with separating interfaces. Above  $T_c$ , the interfacial effects vanish, and the liquids become perfectly miscible. The free-energy density of the system depends not only on the phase field variable  $\phi$  (which describes the system composition), but also on the reduced temperature  $r = (T_c - T)/T_c$  which measures the distance to the critical point described by  $T_c$ . The free energy suffers transformations through  $T_c$  in a way to permit a two-phase system in the subcritical (immiscible) regime and a monophasic in the supercritical (miscible) regime. Numerical simulations in two spatial dimensions have been performed for isothermal problems (with  $r$  as control parameter) as well as for nonisothermal problems with the energy equation describing the temperature distribution. These simulations reveal the behavior of liquid mixtures and droplet coalescence placed in temperature gradients with temperatures continuously varying from  $T < T_c$  to  $T > T_c$ , problems that could be of large interest in phase transitions in micro- and nanofluidics.

DOI: [10.1103/PhysRevFluids.7.064005](https://doi.org/10.1103/PhysRevFluids.7.064005)

### I. INTRODUCTION

In the past decades, there has been a growing demand for supercritical fluids in industrial applications as alternative ecofriendly refrigerants, cold energy storage of liquefied natural gas [1], superconducting magnet cooling [2], chemical extraction/separation processes/polymerization [3–5], and space applications [6–8]. Whereas experimental studies are limited due to complex conditions during their realization, numerical modeling proves to be a useful tool in understanding the fundamental flows and transport characteristics.

We propose and investigate numerically a phase field model able to describe the passage in the limit of a continuous approach of the critical point—from a two-phase subcritical state to a monophasic supercritical state and vice versa. This behavior appears both in a liquid-vapor system and in an immiscible/miscible liquid-liquid system. The last case is the subject of our paper. Suitable binary liquid pairs are considered with the interfacial tension depending on temperature: below a critical temperature  $T_c$ , we have a liquid-liquid immiscible state (two-phase states). Above the critical temperature, the interfacial tension disappears, and the two liquid pairs become perfectly

---

<sup>\*</sup>borciar@b-tu.de

miscible (monophasic state). Around the critical temperature, the thermodynamic and transport properties are modeled as universal power laws on the reduced temperature  $r = (T_c - T)/T_c$  [9]. The parameter  $r$  represents the measure of the distance to the critical point.

One of the major challenges lying in numerical phase field modeling is the vanishing (appearance) of an interface as one continuously moves from subcritical (supercritical) to supercritical (subcritical) states. The phase field approach delivers a continuum thermodynamical model able to treat multiphase problems. An auxiliary variable  $\phi$ —the phase field—is added to the usual set of state variables in order to provide an explicit indication of the system composition.  $\phi$  can be simply a number or can depict a physical property of the system, such as the density, mass, or volume fraction. This parameter takes different values for different phases and exhibits a rapid but smooth variation in the interfacial region. The free energy of the system is an integral of two contributions, one being a function only of the phase field variable  $\phi$  (describing the homogeneous bulk phases) and the other—the “gradient energy”—a term proportional to the square of the local gradient  $\nabla\phi$  (describing the nonhomogeneous interfacial region) [10–14]. Being free of interface conditions, phase field models are very attractive and effective to describe spatially and temporally varying interfaces with complicated geometries. They achieved considerable success in modeling solidification phenomena [15,16], dendritic growths [17,18], static and dynamic contact angles [19–21], controlled drop motion under vibrations [22], drop behavior on noisy surfaces [23], or bubble manipulation by alternating current electrowetting [24].

The investigation in the present paper is based on a conservative phase field model for almost incompressible binary mixtures. The Cahn-Hilliard equation serves as the evolution equation for the phase field variable  $\phi$  [12]. The free-energy density used in this paper depends not only on  $\phi$ , but also on the reduced temperature  $r$ . This fact allows to treat phase transition problems, namely, to permit a continuous change by temperature from a biphasic subcritical system to a monophasic supercritical system and vice versa. Section I presents the theoretical background. Section II shows numerical results in two spatial dimensions for liquid mixtures and coalescing droplets near the critical point. Here, two problems will be analyzed: isothermal problems with the reduced temperature  $r$  acting as a control parameter and nonisothermal problems with  $r$  varying from point to point in the evolving system. In the last case, the energy equation (describing the temperature field) will be included. We gather our conclusions in Sec. III.

## II. THEORETICAL FRAMEWORK

Considering the phase field parameter  $\phi$  proportional to the mass fraction  $\psi$  ( $\phi = 2\psi - 1$ ), the set of governing equations for an immiscible-miscible binary liquid problem reads [12,25]

$$\rho \frac{d\vec{v}}{dt} = -\nabla p - \nabla \cdot (\mathcal{K}\rho \nabla\phi \otimes \nabla\phi) - \frac{\nabla(\mathcal{K}\rho)(\nabla\phi)^2}{2} + \nabla \cdot (\eta \nabla \vec{v}), \quad (1)$$

$$\frac{\partial \rho}{\partial t} = -\nabla \cdot (\rho \vec{v}), \quad (2)$$

$$\frac{d\phi}{dt} = \frac{1}{\rho} \nabla \cdot (M_o \nabla \mu), \quad (3)$$

$$\rho c \frac{dT}{dt} = \nabla \cdot (\kappa \nabla T), \quad (4)$$

where  $p$  represents the pressure field,  $\vec{v}$  is the mass-averaged velocity (barycentric velocity),  $\eta$  is the dynamic viscosity,  $c$  is the specific-heat capacity, and  $\kappa$  is the thermal conductivity (assumed to be constant). The system contains no volumetric heat sources, and the fluids are almost incompressible. The phase field  $\phi$  in the bulk is assumed to be +1 for liquid 1 (having the density  $\rho_1$ ), -1 for liquid 2 (having the density  $\rho_2$ ), and 0 for the supercritical (mixed) state.  $\rho(x, z, t)$  denotes the density,

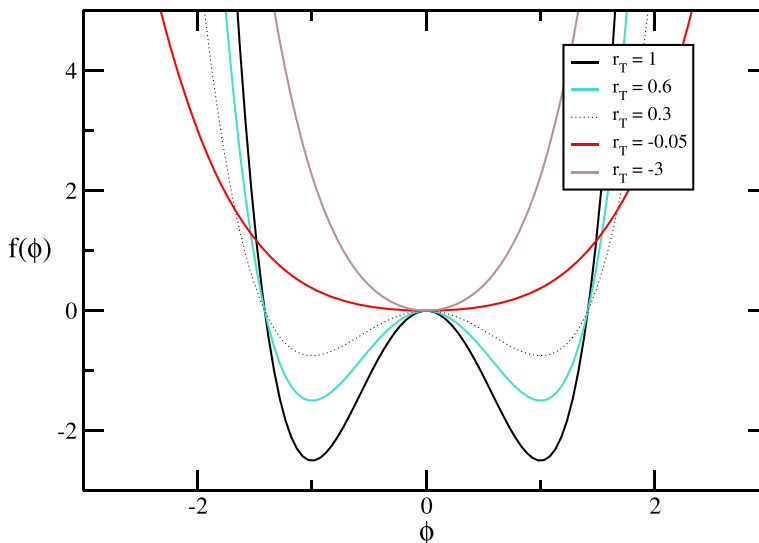


FIG. 1. Transformations of the free-energy density through the critical state (at  $r_T = 0$ ). Immiscible state for  $r_T > 0$  with two local minima at  $\phi = -1$  (liquid 1) and  $\phi = 1$  (liquid 2) and miscible state for  $r_T < 0$  described by the phase field  $\phi = 0$ .

related to the phase field,

$$\frac{1}{\rho} = \frac{1 + \phi}{2\rho_1} + \frac{1 - \phi}{2\rho_2}. \quad (5)$$

$\mu(x, z, t)$  is the chemical potential of the multicomponent system,

$$\mu = \rho \frac{\partial f}{\partial \phi} - \nabla \cdot (\mathcal{K} \rho \nabla \phi), \quad (6)$$

$\mathcal{K}$  is the gradient energy coefficient, and  $M_o$  is a mobility parameter.  $f$  represents the bulk free-energy density (per unit mass),

$$f(\phi, T) = r_0 \left( -\frac{1}{2} r_T \phi^2 + \frac{1}{4} |r_T| \phi^4 \right), \quad (7)$$

with  $r_T$  as a monotonic function of the reduced temperature  $r$  and  $|r_T|$  as the absolute value of  $r_T$ .  $r_0$  is a constant. The free-energy density suffers a transformation through the critical state at  $r_T = 0$  (Fig. 1). For  $r_T > 0$ , the free-energy (7) describes biphasic states corresponding to an immiscible liquid-liquid problem. In this range,  $f$  has the shape of a double-well potential with two local minima at  $\phi = -1$  for liquid 1 and  $\phi = +1$  for liquid 2. Below the critical threshold  $r_T < 0$ , the two liquids become perfectly miscible (binary mixture). For the monophasic supercritical (mixed) states,  $f$  takes the shape of a parabola with the opening to the top and the vertex at  $\phi = 0$ .

For subcritical states, far below the critical point ( $T \ll T_c$ ),  $r$  (and  $r_T$ ) has the value 1 and the gradient energy coefficient  $\mathcal{K}$  is a constant. The two constants  $r_0$  and  $\mathcal{K}$  are related to the surface tension coefficient  $\sigma$  and the interface thickness  $d$ :  $\sigma \propto \sqrt{\mathcal{K} r_0}$ ,  $d \propto \sqrt{\mathcal{K}/r_0}$  [26]. Above the critical point the interface disappears, i.e. the surface tension has to vanish. To include the vanishing of the interface at the critical temperature  $T_c$ , we will choose for the gradient energy coefficient a temperature dependence of the form  $\mathcal{K} \propto r$  and  $r_T$  appearing in the free-energy potential (7):  $r_T \propto r^3$ .

For supercritical states,  $r$  becomes negative, and we assume  $\mathcal{K} = 0$ . In this way the surface tension coefficient  $\sigma \propto \sqrt{\mathcal{K} r_0 r_T}$  acts only for subcritical states with a dependence of the form

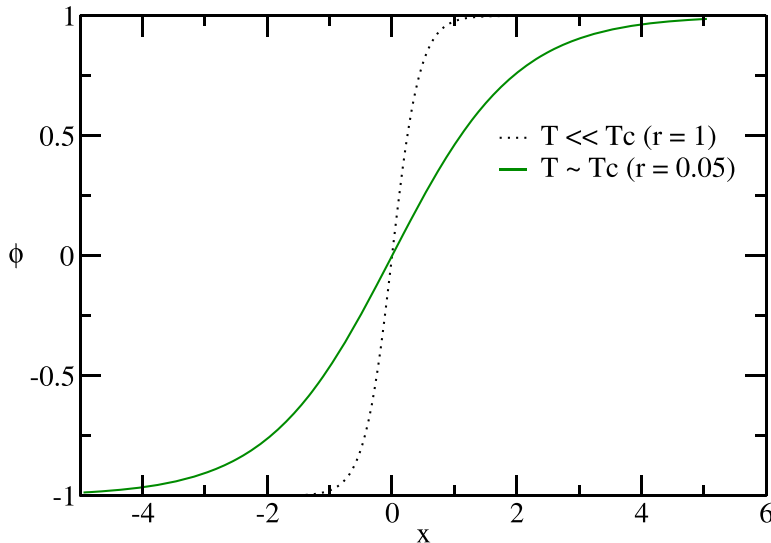


FIG. 2. Divergence of the liquid-liquid interfacial thickness near the critical point.

$\sigma \propto r^2$  and becomes zero at the critical point. With this choice as expected, the interfacial thickness  $d \propto \sqrt{\mathcal{K}/(r_0 r_T)} \propto 1/r$  asymptotically diverges at the critical point (see Fig. 2) [9].

The phase field equation [Cahn-Hilliard equation, (3)] can be easily derived from the mass balance equation of one of the components of the binary mixture,

$$\frac{\partial(\rho\phi)}{\partial t} + \nabla \cdot (\rho\phi\vec{v}) = \nabla \cdot \vec{j}_d, \quad (8)$$

where  $\vec{j}_d$  represents the diffusional flux. After some mathematical manipulations, the above equation writes

$$\rho \left( \frac{\partial\phi}{\partial t} + \vec{v} \cdot \nabla\phi \right) + \phi \left( \frac{\partial\rho}{\partial t} + \nabla \cdot (\rho\vec{v}) \right) = \nabla \cdot \vec{j}_d. \quad (9)$$

According to the continuity equation (2), the second bracket in (9) is zero. The diffusive flux is attributed to the gradient of the chemical potential  $\mu$  which exists near the interface region for a smooth transition of the phase field  $\phi$  from one phase to another. Thus, with  $\vec{j}_d = M_o \nabla\mu$ , Eq. (9) results in the Cahn-Hilliard equation with advection (3). For supercritical states, the gradient energy coefficient  $\mathcal{K}$  is 0, transforming the Cahn-Hilliard equation (3) into a diffusion equation describing the mixing of two miscible components.

### III. NUMERICAL RESULTS

We scale the variables by using  $d$ ,  $d^2/\nu$ ,  $\nu/d$ ,  $\rho_1$ ,  $\rho_1 v^2/d^2$ ,  $\nu/r_0$ , and  $T_c$  as units for the length, time, velocity, density, pressure, mobility, and temperature, where  $\nu = \eta/\rho_1$  is the kinematic viscosity of the liquid 1.  $T_c$  is, for example, for the pair of liquids 1 cSt silicon oil ( $\rho = 880 \text{ kg/m}^3$ ) and FC-72 perfluorohexane ( $\rho = 1580 \text{ kg/m}^3$ ) 42 °C [27]. We use in this paper  $\rho_1 = 800$ ,  $\rho_2 = 1600 \text{ kg/m}^3$ ,  $\nu = 10^{-6} \text{ m}^2/\text{s}$  (for both liquids),  $\mathcal{K} = \mathcal{K}_0 r$ ,  $\mathcal{K}_0 \rho_1 = 1.6 \times 10^{-10} \text{ N}$ ,  $r_0 \rho_1 = 1.6 \times 10^2 \text{ N/m}^2$ . It follows for the thickness of the diffuse interface  $d = \sqrt{\mathcal{K}_0/r_0} = 10^{-6} \text{ m}$  and the surface tension coefficient  $\sigma = \rho_1 \sqrt{\mathcal{K}_0 r_0} = 0.16 \text{ mN/m}$ . The scaled time is  $10^{-6} \text{ s}$ .

After scaling the following nondimensional parameters appear:  $Ca = v^2/\mathcal{K}_0$ — the capillary number,  $Pr = \eta c/\kappa$  the Prandtl number, and  $\tilde{M}_o = M_o r_0/\nu$  is the scaled mobility. For the numerical results presented in this paper,  $Ca = 5$ ,  $Pr = 5$ , and  $\tilde{M}_o = 1$ .

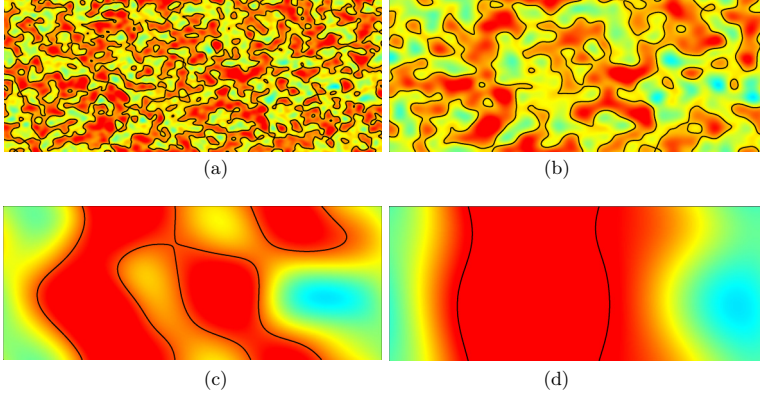


FIG. 3. Mixing and diffusion in the supercritical state: (a)  $t = 0.1$ ; (b)  $t = 0.5$ ; (c)  $t = 10$ ; (d)  $t = 40$ . In a late state of evolution  $\rho/\rho_1 = 1.333$  ( $\phi = 0$ ). The contour lines follow the isolines having  $\rho/\rho_1 = 1.333$ . The scaled time is  $10^{-6}$  s, the box size is  $400 \times 200$ , and the scaled length is  $10^{-6}$  m.

As the numerical method a centered finite-difference method (second-order approximation) is applied on Eqs. (1), (3), and (4) under periodic boundary conditions in the horizontal ( $x$ ) and vertical ( $z$ ) directions [28,29]. For each iteration step, the density field  $\rho$  follows the changes of the phase field  $\phi$ , according to relation (5). For all presented figures the meshes are  $400 \times 200$  points (with the distance between two mesh points  $\Delta x = \Delta z = 1$ ) except for Fig. 4 which has a resolution of  $200 \times 200$  ( $\Delta x = \Delta z = 1$ ) and Fig. 8 which has a resolution of  $104 \times 52$  ( $\Delta x = \Delta z = 0.4$ ). For time integration we use an Euler method. The time step is restricted at  $\Delta t < \Delta x^2$  due to numerical instability given by the explicit terms and accuracy. In our runs, we fix  $\Delta t = 0.01$ , assuring in this way a numerical stability of the codes.

From the relations (3) and (5), we easily get

$$-\frac{1}{\rho^2} \frac{d\rho}{dt} = \frac{\rho_2 - \rho_1}{2\rho_1\rho_2} \frac{d\phi}{dt} = \frac{\rho_2 - \rho_1}{2\rho_1\rho_2} \frac{1}{\rho} \nabla \cdot (M_o \nabla \mu) = \frac{\rho_2 - \rho_1}{2\rho_1\rho_2} \frac{1}{\rho} \nabla \cdot \vec{j}_d.$$

Combining the above relation with the continuity equation (2), it follows:

$$\nabla \cdot \vec{v} = -\frac{1}{\rho} \frac{d\rho}{dt} = \frac{\rho_2 - \rho_1}{2\rho_1\rho_2} \nabla \cdot (M_o \nabla \mu) = G(\mu). \quad (10)$$

The relation (10) shows that the velocity field is not solenoidal because of the existent diffusional flux  $\vec{j}_d = M_o \nabla \mu \neq 0$ .

In order to get a conservative system, the discretized momentum equation for “ $i$ ” component (with  $i = x, z$ ) is solved in two steps [30,31],

$$\frac{v_i^* - v_i(t)}{\Delta t} = -(\vec{v} \cdot \nabla)v_i + \frac{\partial \Xi_{ij}}{\partial x_j}, \quad (11)$$

$$\frac{v_i(t + \Delta t) - v_i^*}{\Delta t} = -\frac{1}{\rho} \frac{\partial p}{\partial x_i}, \quad (12)$$

where  $\vec{v}^*$  is the “viscous” component of the velocity field and  $\Xi_{ij}$  is the generalized viscous stress tensor including the Korteweg stress components from (1).

Using (10), we enforce the continuity equation at each time step,

$$\nabla \cdot \vec{v}|_{t+\Delta t} = G(\mu)|_{t+\Delta t}. \quad (13)$$

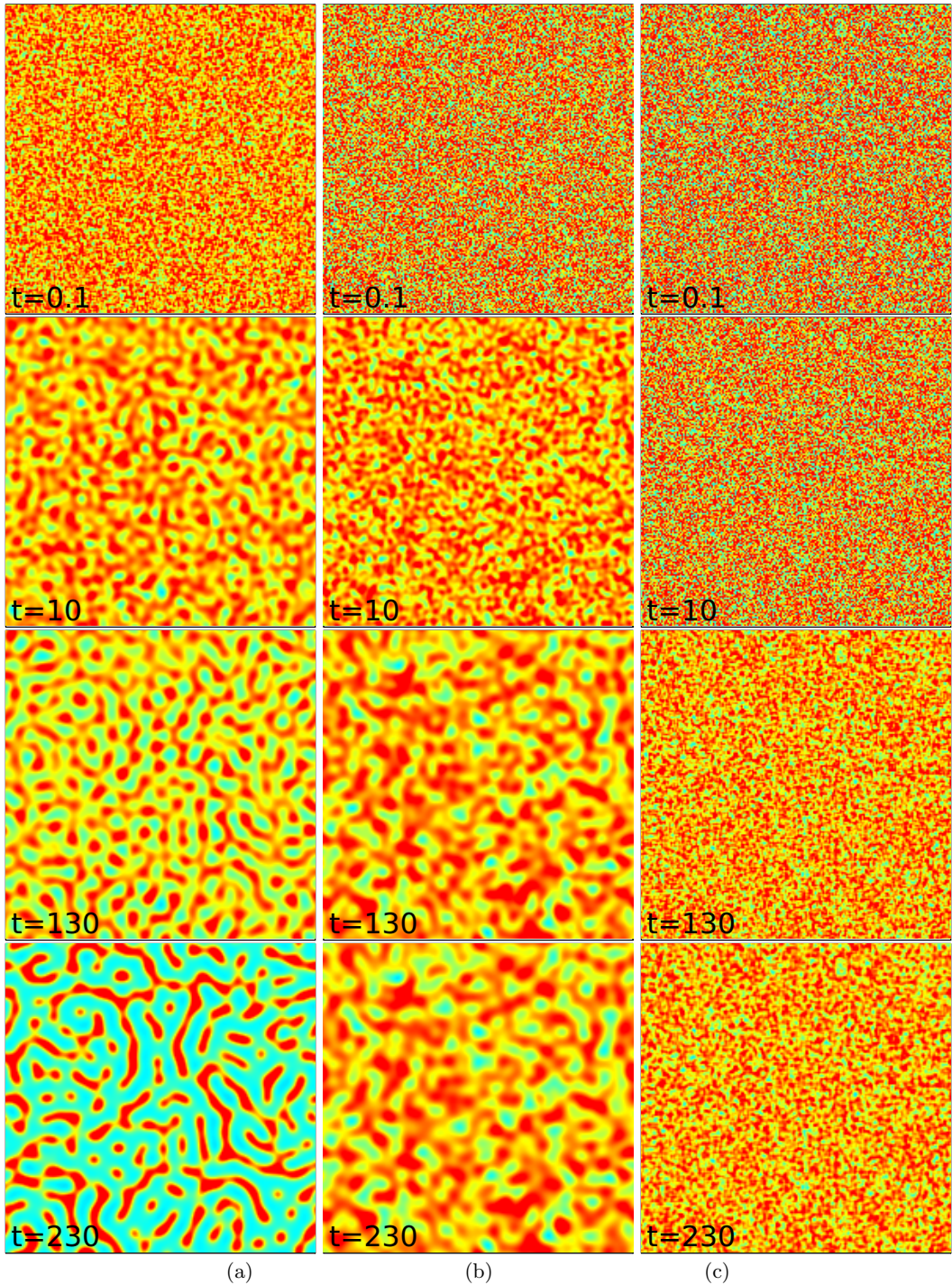


FIG. 4. Time series (at same moments) for phase separation: (a) far away from the critical point  $r = 1$  and closer to critical point (b)  $r = 0.1$ , and (c)  $r = 0.001$ , respectively. From the top to the bottom the moment of times are correspondingly:  $t = 0.1$ ,  $t = 10$ ,  $t = 130$ , and  $t = 230$ . Approaching the critical point, the coarsening becomes slower and weaker (the capillary effects almost disappear). The scaled time is  $10^{-6}$  s, the box size is  $200 \times 200$ , and the scaled length is  $10^{-6}$  m.

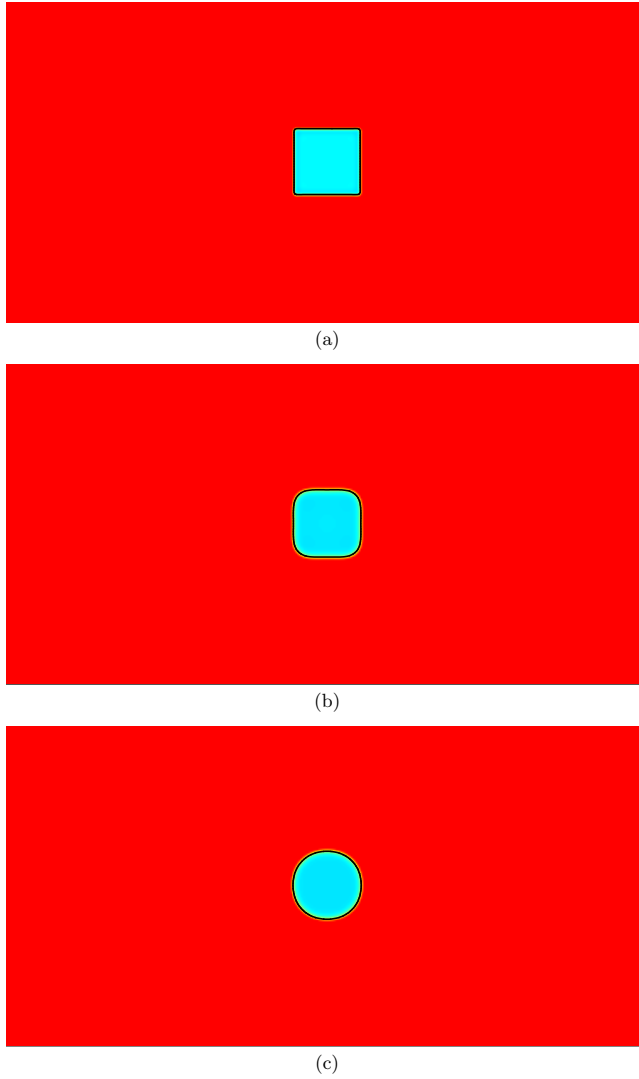


FIG. 5. Drop formation from its initial square shape due to capillary forces at the liquid-liquid interfaces far below the subcritical threshold  $r = 1$ . The formed drop has a density  $\rho/\rho_1 = 1$  and is surrounded by a liquid with  $\rho/\rho_1 = 2$ . The snapshots correspond to the moments: (a)  $t = 0.8$ ; (b)  $t = 45$ ; (c)  $t = 110$ , respectively. The initial square is of size  $40 \times 40$ . The interface is abrupt and is not a solution of the problem. After relaxation, the interface becomes diffuse, and this is a solution of the problem. In panel (c), the formed circle has a radius of 42.4. The scaled time is  $10^{-6}$  s, the box size is  $400 \times 200$ , and the scaled length is  $10^{-6}$  m.

Applying the divergence in (12), one obtains

$$\frac{1}{\Delta t} [\nabla \cdot \vec{v}(t + \Delta t) - \nabla \cdot \vec{v}^*] = -\nabla \cdot \left( \frac{\nabla p}{\rho} \right). \quad (14)$$

From (13) and (14) we find now the generalized Poisson equation for the pressure field,

$$\nabla \cdot \left( \frac{\nabla p}{\rho} \right) = \frac{1}{\Delta t} [\nabla \cdot \vec{v}^* - G(\mu)]. \quad (15)$$

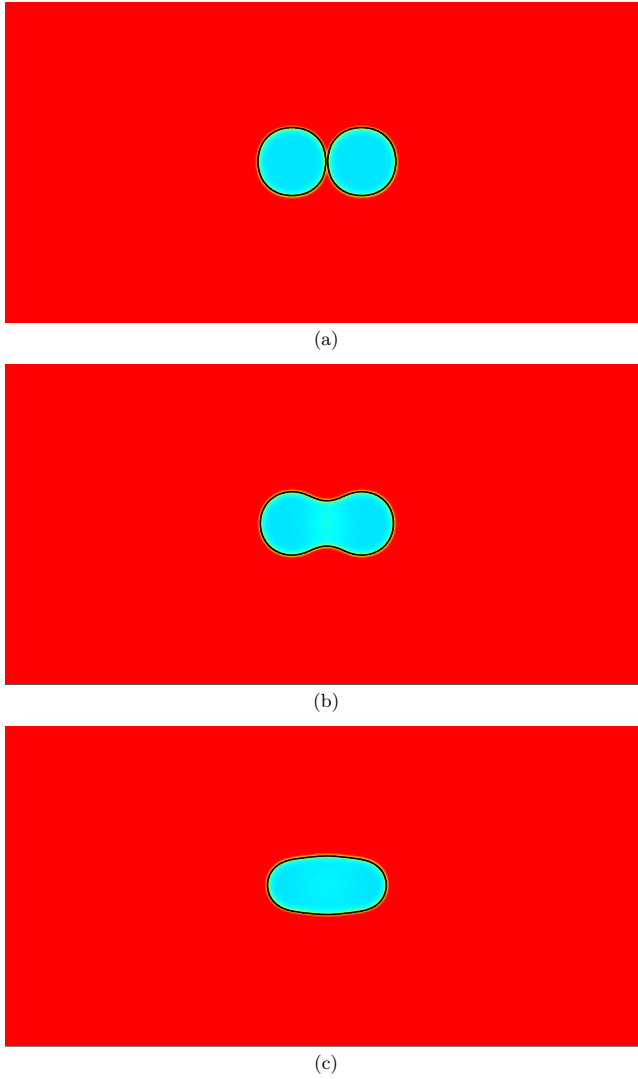


FIG. 6. Coalescence of twin drops of radius 42.4 far from subcritical threshold ( $r = 1$ ). The bridging film grows in time in transversal direction until the minimum between the connecting droplets disappears: (a)  $t = 0.5$ ; (b)  $t = 100$ ; (c)  $t = 200$ . The scaled time is  $10^{-6}$  s, the box size is  $400 \times 200$ , and the scaled length is  $10^{-6}$  m.

Equation (15) is solved using an iterative method,

$$p^{(n+1)} = p^{(n)} + \left[ \nabla \cdot \left( \frac{\nabla p}{\rho} - \frac{\vec{v}^*}{\Delta t} \right) + \frac{G(\mu)}{\Delta t} \right] \lambda,$$

with  $\lambda$  as a chosen parameter (relaxation factor). The iteration loop is performed until the correction,

$$\sum_{i,j} |p_{i,j}^{(n+1)} - p_{i,j}^{(n)}|$$

drops below a desired accuracy  $\epsilon$  (with  $i$  and “ $j$ ” denoting the discretization indices in the  $x$  and  $z$  directions). For the parameters indicated in this paper, less than 25 iterations for each time step are



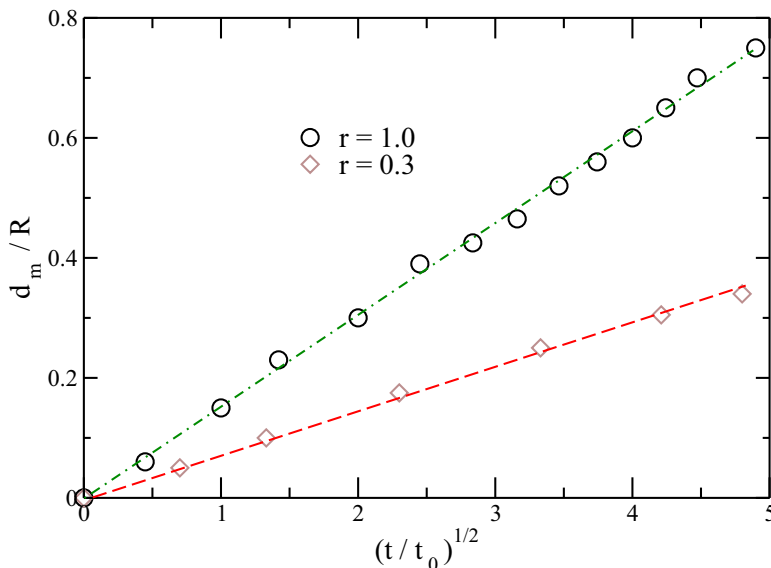


FIG. 7. Time evolution of the bridge film in the transversal direction during the coalescence process for two reduced temperatures  $r$ . The connecting neck between the interacting drops increases linearly with  $t^{1/2}$ , according to Aarts *et al.* [34]. The green dashed-dot and red dashed lines are the linear interpolations of the points from the numerical experiment crossing the origin.

enough to reach the final solution. That means 2 to 3 h for one complete simulation run, working on a single core unit equipped with a 3.6 GHz Intel Core™ i7-4790 processor. The corrected pressure field  $p$  is now used to calculate the velocity field  $\vec{v}^*$  at the next time moment in Eq. (1).

#### A. Isothermal case

We analyze the behavior of a liquid mixture at constant temperature. As an initial condition, we consider in each case the phase field variable  $\phi$  as a uniformly random-distribution ranging between  $-0.01$  and  $0.01$ . At  $t = 0$  the liquid mixture is at rest. The density field distributions are investigated for two situations: the behavior of the liquid mixture in the supercritical regime for  $r = -1$  (Fig. 3) and in the subcritical regime for, respectively,  $r = 1$ ;  $0.1$ ;  $0.001$  (Fig. 4). In the supercritical regime, the surface tension is not acting. The phase field equation (3) turns into a diffusion equation describing the mixing of two miscible components. Therefore, in this case one assists to diffusion and mixing. To assure a good contrast in all our density field plots, for each snapshot the colors are rescaled from the actual minima (blue) to the actual maxima (red). Our color scale is explicitly shown in Fig. 17. In Fig. 3(d), the red color designates  $\rho/\rho_1 = 1.334$ , and the blue color designates  $\rho/\rho_1 = 1.332$ . So, after  $t = 40$ , even in Fig. 3(d) due to high contrast scaling we can distinguish different colors. In fact, we have an almost completely mixed composition described by the phase field  $\phi \approx 0$ , having the density  $\rho/\rho_1 \approx 1.333$ .

The achieving of the complete mixing of the two components with the mixture density  $\rho/\rho_1 \approx 1.333$  represents the validation of our numerical simulations for the supercritical regime.

In the subcritical regime, we plot density field snapshots at the same moments for different  $r$  reduced temperatures. Phase separation and coarsening phenomena occur with stronger separation rates far below the critical point. Approaching the critical point ( $r \rightarrow 0$ ), the coarsening becomes slower and weaker because the capillary effects almost disappear. Instead for  $r = 1$  in Fig. 4—these phenomena look very strong at  $t = 230$  where the phase fields are ranging already from  $-1$  ( $\rho/\rho_1 = 2$ , red zones) to  $+1$  ( $\rho/\rho_1 = 1$ , blue zones). In contrast to Fig. 4(a), Fig. 4(c) reveals for

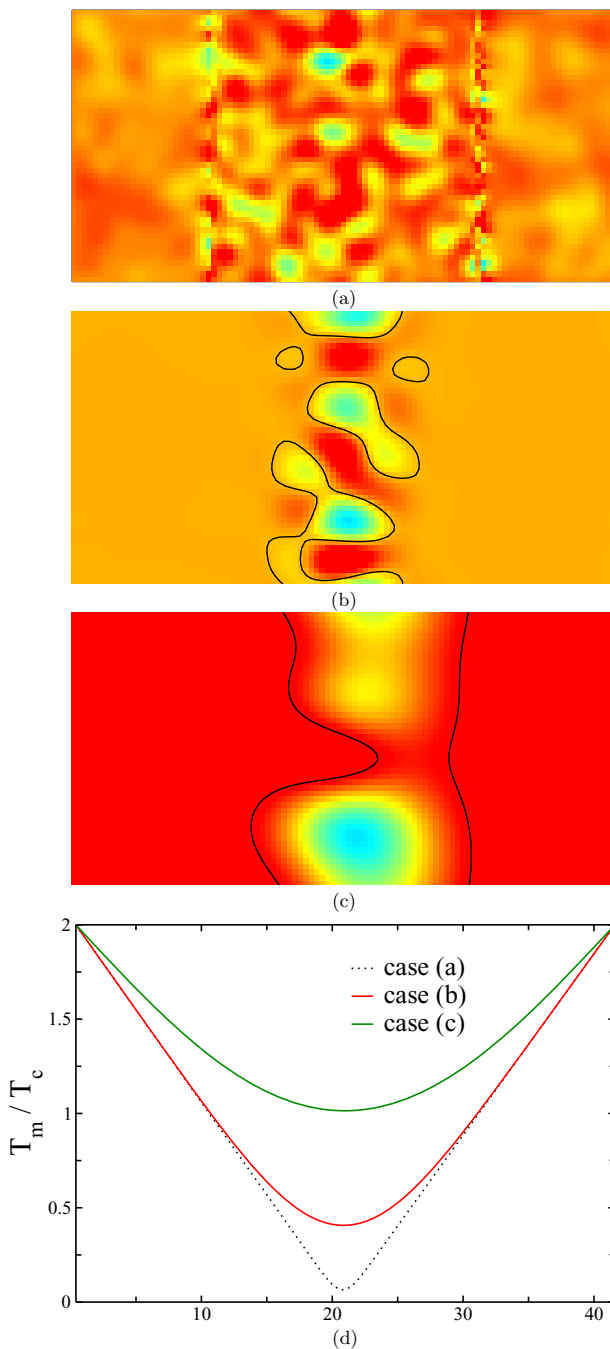


FIG. 8. Phase separation in temperature gradient for strong thermal diffusion in the system: (a)  $t = 0.5$ ; (b)  $t = 460$ ; (c)  $t = 2860$ . The corresponding temperature fields  $T_m$  (averaged in the vertical direction) are plotted in panel (d). The scaled time is  $10^{-6}$  s and the scaled length  $10^{-6}$  m.

$r = 0.001$  very little changes in the density field distribution for  $t = 230$  comparing with the initial moment.

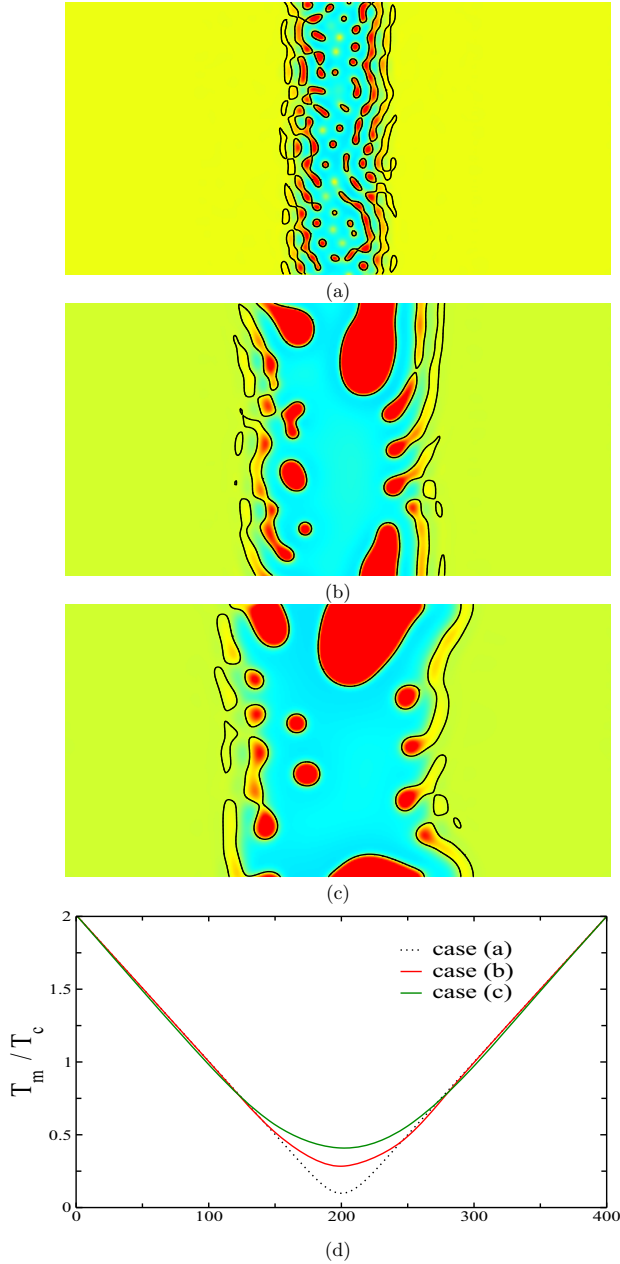


FIG. 9. Phase separation in temperature gradient for lower thermal diffusion in the system: (a)  $t = 1500$ ; (b)  $t = 10000$ ; (c)  $t = 25000$ . See the movie in the Supplemental Material [35] for the time evolution of the phase separation process. The corresponding temperature fields  $T_m$  (averaged in the vertical direction) are plotted in panel (d). The scaled time is  $10^{-6}$  s and the scaled length  $10^{-6}$  m.

For the validation of our numerical simulation in the subcritical regime, we consider two known configurations [32,33]. We examine the coalescence of two identical free drops in the immiscible subcritical regime ( $r = 1$ ). First, we get the circle drop starting from a square shape [33]. With the time, the initial structure from Fig. 5(a) will be rounded by capillary forces, obtaining a perfectly

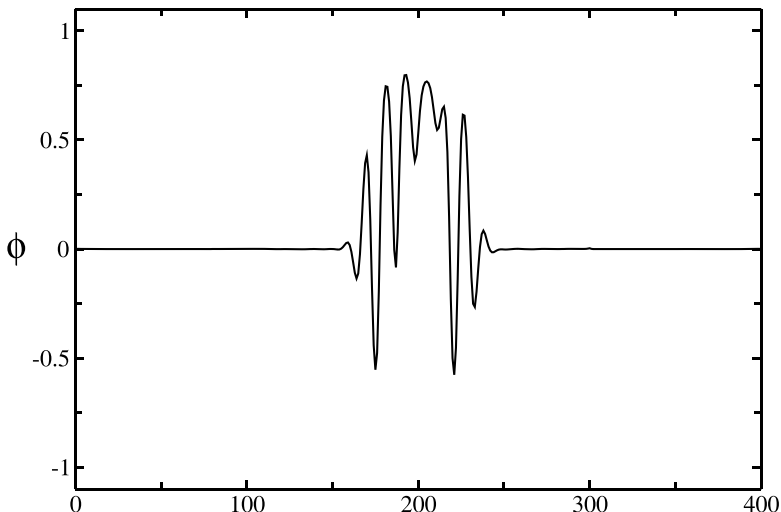


FIG. 10. Phase field distribution in horizontal direction at 3/4 of the  $z$  length in Fig. 9(a).

spherical droplet with  $\phi = +1$ ,  $\rho/\rho_1 = 1$  in the surrounding liquid with  $\phi = -1$ ,  $\rho/\rho_1 = 2$  [see Fig. 5(c)]. As a second numerical validation experiment, we take two drops approaching each other until their contact lines become close enough to initiate the coalescence process [32]. That means the system favors the merging of the drops to reduce the total surface area and in this way minimize the free energy, forming in a late state of evolution a single rounded liquid droplet. The viscous forces slow the coalescence process down. The fusion process consists of two stages: A growth of the meniscus bridge connecting the two drops (see the snapshots displayed in Fig. 6) followed by a rearrangement of the combined droplet shape from an elliptical to a circular shape. The second stage is not shown in the present paper. We investigate the time dependence of the growth of the width of the connecting neck between the drops in early-time evolution until the minimum between the coalescing droplets disappears. The width of the bridging meniscus  $d_m$  is taken from two-dimensional phase field plots, following the location of the interface given by the contour line  $\phi = 0$ . The increase in the connecting neck between the coalescing droplets shows a  $t^{1/2}$  dependence, specific for the low viscosity regime, a very good agreement with the power-law behavior reported by Aarts *et al.* [34]. The droplet radius  $R$  corresponds to a reference moment  $t_0$  ( $t_0 = 4.5$ ) during the coalescence process. The linear dependencies (with  $t^{1/2}$ ) have been plotted for different reduced temperatures  $r$  (green dashed-dot and red dashed lines Fig. 7). As one can see in Fig. 7, the slope is higher for the case far below the critical point ( $r = 1$ ) because the contribution of capillary forces is stronger, and, therefore, the coalescence process becomes faster. Also, quantitatively, we achieve a very good agreement with the Aarts's theory [34] regarding the hydrodynamics of droplet coalescence. So, the slope ratio corresponding to the two linear functions plotted in Fig. 7 is  $\approx 1.9$ . On the other side, from the relation (2) in Ref. [34], the same ratio is given by  $(\sigma_1/\sigma_2)^{1/4}$ , where  $\sigma_1$  and  $\sigma_2$  are, respectively, the surface tension coefficients for the two cases. That means in our model in terms of reduced temperatures  $(r_1/r_2)^{1/2}$ , namely,  $(1/0.3)^{1/2} \approx 1.83$ .

### B. Nonisothermal case

We consider now a liquid mixture (with  $\phi$  uniformly random-distributed ranging between  $-0.01$  and  $0.01$ ) placed in a temperature gradient. Laterally the temperature is kept constant  $T/T_c = 2$ . At the initial moment  $t = 0$ , the system is at rest and the temperature field presents a linear variation with the minimum  $T = 0$  in the middle of  $x$  length ( $x = 200$ ). In this way, we have simultaneously in the system both subcritical ( $T < T_c$ ,  $r > 0$ ) and supercritical regimes ( $T \geq T_c$ ,  $r \leq 0$ ) with  $r$  continuously varying from  $r = 1$  to  $r = -1$ . Figures 8 and 9 display two-dimensional density

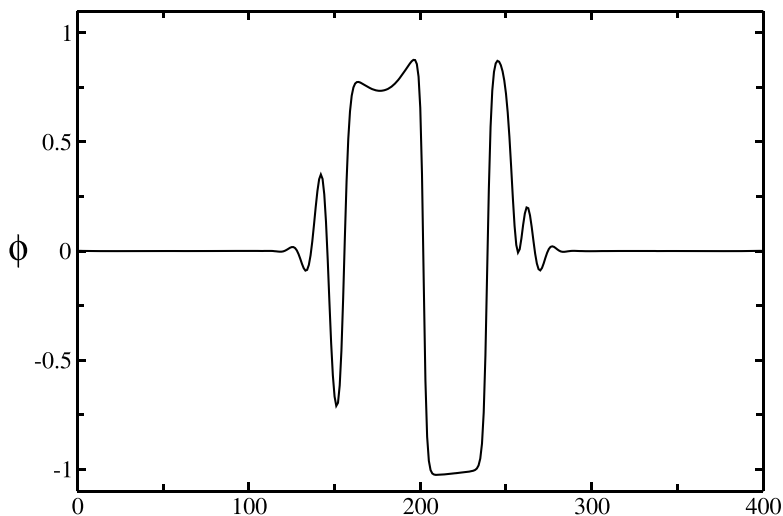


FIG. 11. Phase field distribution in the horizontal direction at 3/4 of the  $z$  length in Fig. 9(b).

distributions and corresponding temperature fields (averaged in vertical direction) for two different sizes of the box:  $0.041 \times 0.02 \text{ mm}^2$  and  $0.4 \times 0.2 \text{ mm}^2$ , respectively. Because the thermal diffusion time is proportional to the square of the box length, large systems have large thermal diffusion times and vice versa. Stronger capillaries (higher  $r$  parameters,  $r > 0$ ) enhance the phase separation. In regions with temperatures  $T > T_c$  ( $r < 0$ ), the capillarity effects vanish. In subcritical regimes, two processes are in competition: phase separation/coarsening (stronger in the zones with higher  $r$ ) and thermal diffusion (see Figs. 8 and 9). In Fig. 8 (for small system with small thermal diffusion time), in the central regions phase separation starts with phase fields of order  $10^{-2}$ . The phase field reaches 0.4 in Fig. 8(b) and decreases afterwards one order of magnitude from  $t = 460$  to  $t = 2860$  [see Fig. 8(c)]. This is due strong thermal diffusion which leads to a rapid increase of the temperatures above  $T_c$  [see Fig. 8(d)]. For  $T > T_c$  ( $r < 0$ ), diffusion and mixing occur in the entire system. Instead

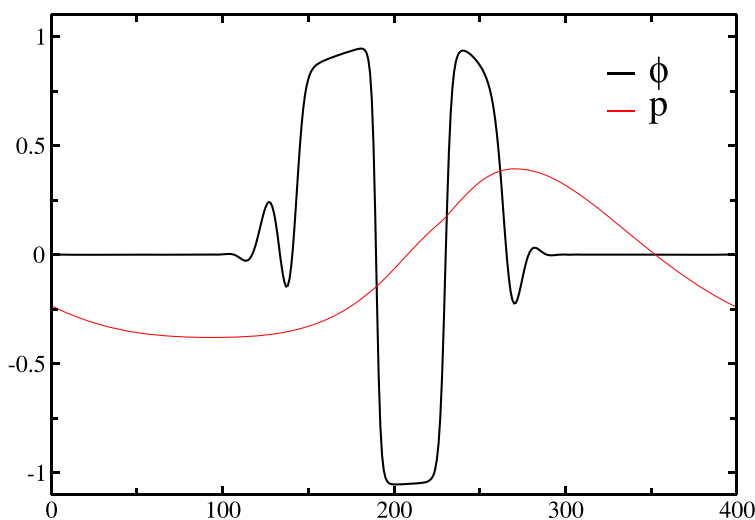


FIG. 12. Phase field and scaled pressure distribution at 3/4 of the  $z$  length in the horizontal direction in Fig. 9(c).

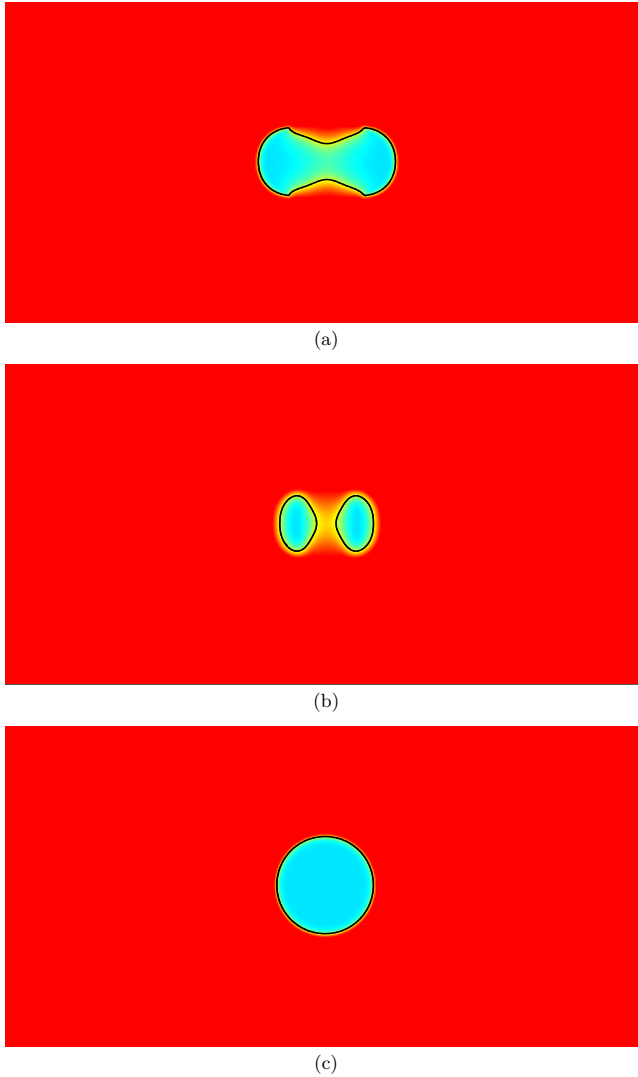


FIG. 13. Coalescing drops in temperature gradient at: (a)  $t = 100$ ; (b)  $t = 4900$ ; (c)  $t = 900\,000$ . We start from two twin droplets of radius 42.4. Here the end state is a bigger droplet of radius 59.6. We note that both initial and final states are solutions of the problem and, thus, their ratio  $59.6/42.4$  is very close to  $\sqrt{2}$ , which proves a very good mass conservation in the system. The scaled time is  $10^{-6}$  s, the box size is  $400 \times 200$ , and the scaled length is  $10^{-6}$  m.

for lower thermal diffusion in the system, Fig. 9 shows strong phase separations, phase fields varying from  $-1$  and  $+1$  and the densities  $\rho/\rho_1$ , correspondingly, from 2 and 1. Rounded droplets are observed in the middle regions and later on strong coarsening phenomena occur (see also Figs. 10 and 11, presenting the horizontal phase field distributions for the snapshots depicted in Figs. 9(a) and 9(b) at  $3/4$  of the  $z$  length). From all the situations presented in this paper, the pressure forces play an essential role in the case shown in Fig. 9 where the created pressure force in the system stops the expansion of the separation front in the lateral direction (Fig. 12). In the regions with  $T > T_c$ , mixing phenomena is observed, finally the temperature rises in the entire system over  $T_c$ , and we get an almost completely mixed liquid (supercritical state). The full dynamics of the situations depicted

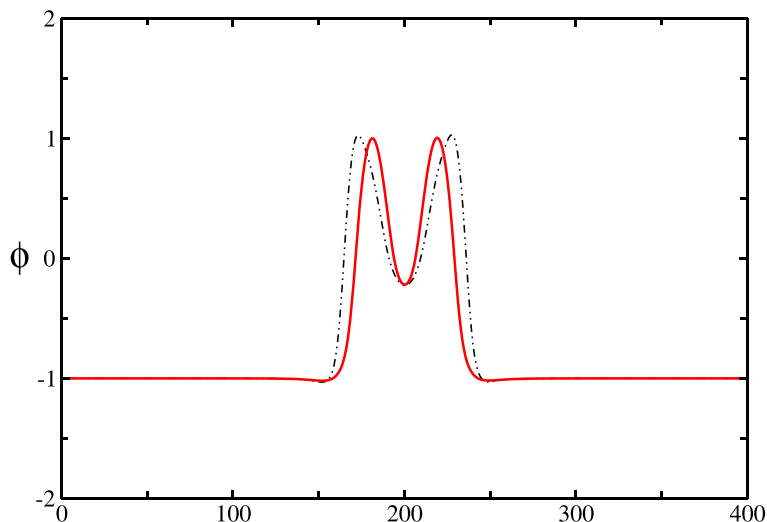


FIG. 14. Center-to-center phase field profiles at two different moments of times during the coalescence process:  $t = 100$  (dashed line) and  $t = 4900$  (red straight line). The scaled time is  $10^{-6}$  s, and the scaled length is  $10^{-6}$  m.

in Fig. 9 can be followed through a movie available as the Supplemental Material [35]. From this movie one can easily see the role of the pressure force in the lateral expansion of the separation front.

Next, we analyze the coalescence of twin drops in a temperature gradient with initial temperatures at  $t = 0$  varying linearly from subcritical ( $T = 0$  on lateral sides) to supercritical regimes ( $T/T_c = 1.125$  in the middle of  $x$  length at  $x = 200$ ). The two coalescing droplets having  $\rho/\rho_1 = 1$  are inserted in the liquid volume with  $\rho/\rho_1 = 2$  at  $T/T_c = 1.125$ . We follow the coalescence process, respectively, two-dimensional density distribution, center-to-center phase field profiles, and temperature distributions slightly above the coalescing drops at  $3/4$  of the  $z$  length (Figs. 13–15).

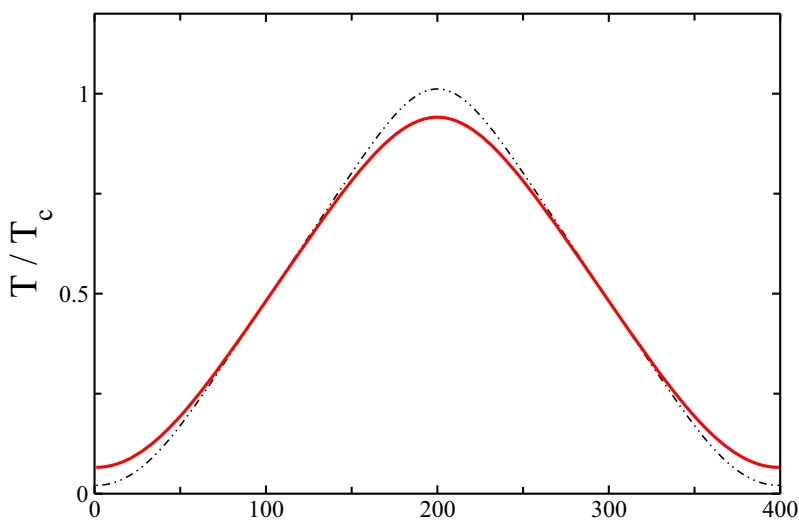


FIG. 15. Temperature profiles for the situations plotted in Fig. 14 slightly above the interacting area at  $3/4$  of the  $z$  length. The scaled time is  $10^{-6}$  s, and the scaled length is  $10^{-6}$  m.

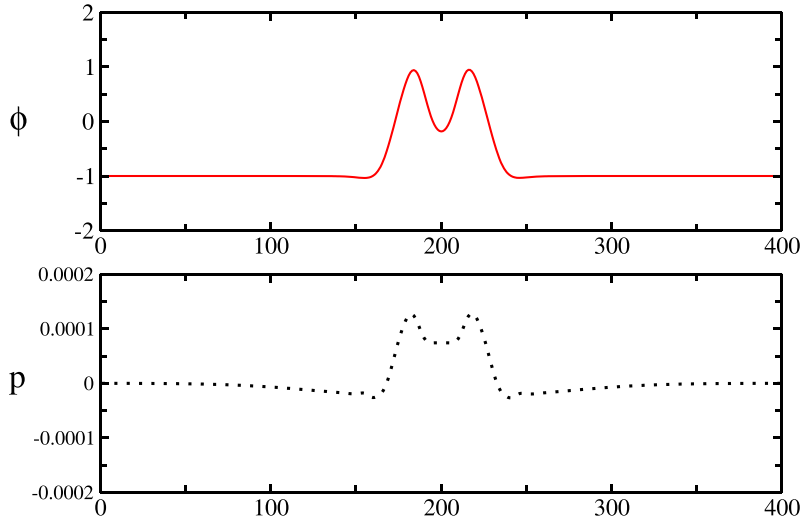


FIG. 16. Phase field and scaled pressure distribution in horizontal direction at midline plane of the  $z$  axis in Fig. 13(b).

One sees that the middle regions are in the supercritical regime, the capillary forces become zero [no rounded lines in the middle area can be observed in Fig. 13(a)]. Furthermore, characteristic for the supercritical regime, mixing of the two components is occurring. Due to temperature diffusion, the temperature decreases in the interaction area of the two drops and increases on the lateral sides (Fig. 15). When the temperature in the interaction area becomes lower than  $T_c$ , the system reaches again the immiscible subcritical regime, and the surface tension gains its significance back. The two components start to separate again and the droplets approach each other (Fig. 14) followed by coalescence [Fig. 13(c)]. Comparing with Fig. 6, the phenomena shown in Fig. 13 reveal a delayed coalescence similar to the phenomena described in earlier papers [36,37], observed during the coalescence of sessile drops from different but perfectly miscible liquids. For the droplet

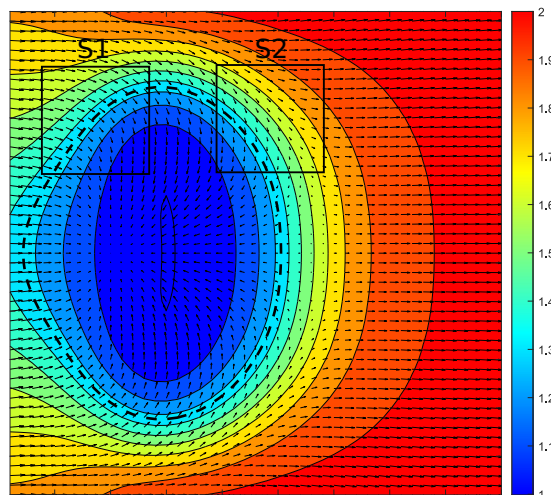


FIG. 17. Density field and barycentric velocity field in the frame of reference of the right-hand-side droplet shown in Fig. 13(b).



coalescence, the velocities are much smaller (two orders of magnitude smaller) as in the situations illustrated in Fig. 10, making also the role of pressure forces less important for this case. Plotting the pressure field for Fig. 13(b), one remarks the increase in pressure under the droplet cape (Laplace pressure) (Fig. 16), shown also in Fig. 7 in Ref. [38] using the thermodynamic pressure term proposed by Jacqmin in Ref. [20]. Quantitatively, the pressure peak of  $0.08 \text{ N/m}^2$  from Fig. 16 is in a very agreement with the Laplace pressure  $\Delta p_L = \sigma r^2/R$ , where  $R$  represents the droplet radius ( $R = 20 \times 10^{-6} \text{ m}$ ,  $r = 0.1$ ).

Figure 17 presents the (barycentric) velocity field in the frame of reference of the right-hand-side droplet shown in Fig. 13(b). One sees the component separation under the influence of Marangoni effects given by the tangential components of the Korteweg stress created by temperature gradients inside the system. Inside the square  $S_1$  in Fig. 17 one has an almost mixed fluid. The surface tension is very low, and one can observe that the velocity field is almost perpendicular to the constant density level lines. On the other side of the same drop (in  $S_2$ ) the capillary forces are much stronger. The Marangoni forces are important and the velocity field becomes more tangential to the density level surface.

#### IV. CONCLUSIONS

The main gain of our paper is to propose a phase field model for immiscible/miscible fluids which permits the description of the continuous path from the two-phase to the monophasic state and vice versa. This is a paper examining coexisting immiscible and miscible states in the same nonisothermal system. Numerical simulations in two spatial dimensions based on this model are able to present the phenomena occurring in a liquid mixture on both sides of the critical point: phase separation/coarsening in the subcritical regime versus diffusion/mixing in the supercritical regime. Droplet coalescence in temperature gradients has also been investigated. We made predictions about droplet shapes and droplet behavior at the boundary between sub- and supercritical domains, a problem that could be of large interest for phase transitions in micro- and nanofluidics. The situations illustrated in Fig. 13 pave the way for more studies dealing with controlled drop motion near the immiscible/miscible critical point. The method presented in this paper can be straightforwardly extended to three spatial dimensions what we plan to do in the future.

#### ACKNOWLEDGMENT

This work was supported by Deutsche Forschungsgemeinschaft (DFG) under the Project “Phase field modeling in phase transition problems.”

- 
- [1] A. Nakano and M. Shiraishi, Numerical simulation for the piston effect and thermal diffusion observed in supercritical nitrogen, *Cryogenics* **44**, 867 (2004).
  - [2] K. Dobashi, A. Kimura, Y. Oka, and S. Koshizuka, Conceptual design of a high temperature power reactor cooled and moderated by supercritical light water, *Ann. Nucl. Energy* **25**, 487 (1998).
  - [3] J. Peter *et al.*, Microgravity phase separation near the critical point in attractive colloids, in *45th AIAA Aerospace Sciences Meeting and Exhibit*, Reno, Nevada, January 2007.
  - [4] A. S. Kaplitz, M. E. Mostafa, S. A. Calvez, J. L. Edwards, and J. P. Grinias, Two-dimensional separation techniques using supercritical fluid chromatography, *J. Sep. Sci.* **44**, 426 (2021).
  - [5] K. Tutek, A. Masek, A. Kosmalka, and S. Cichosz, Applications of fluids in supercritical conditions in the polymer industry, *Polymers* **13**, 729 (2021).
  - [6] S. Amiroudine and D. Beysens, Thermovibrational instability in supercritical fluids under weightlessness, *Phys. Rev. E* **78**, 036325 (2008).
  - [7] D. Sharma, A. Erriguible, and S. Amiroudine, Cooling beyond the boundary value in supercritical fluids under vibration, *Phys. Rev. E* **96**, 063102 (2017).

- [8] S. V. Diwakar, V. Jajoo, S. Amiroudine, S. Matsumoto, R. Narayanan, and F. Zoueshtiagh, Influence of capillarity and gravity on confined Faraday waves, *Phys. Rev. Fluids* **3**, 073902 (2018).
- [9] D. Jasnow, Critical phenomena at interfaces, *Rep. Prog. Phys.* **47**, 1059 (1984).
- [10] J. W. Cahn and J. E. Hilliard, Free energy of a nonuniform system. I. Interfacial free energy, *J. Chem. Phys.* **28**, 258 (1958).
- [11] D. M. Anderson, G. B. McFadden, and A. A. Wheeler, Diffuse–interface methods in fluid mechanics, *Annu. Rev. Fluid Mech.* **30**, 139 (1998).
- [12] J. Lowengrub and L. Truskinovsky, Quasi–incompressible Cahn–Hilliard fluids and topological transitions, *Proc. R. Soc. London A* **454**, 2617 (1998).
- [13] D. Jasnow and D. Vinals, Coarse–grained description of thermo–capillary flow, *Phys. Fluids* **8**, 660 (1996).
- [14] L. M. Pismen and Y. Pomeau, Disjoining potential and spreading of thin liquid layers in the diffuse–interface model coupled to hydrodynamics, *Phys. Rev. E* **62**, 2480 (2000).
- [15] J. S. Langer, Models of patterns formation in first–order phase transitions, in *Directions in Condensed Matter*, edited by G. Grinstein and G. Mazenko (World Scientific, Singapore, 1986), p. 165.
- [16] D. M. Anderson, G. B. McFadden, and A. A. Wheeler, A phase–field model of solidification with convection, *Physica D* **135**, 175 (2000).
- [17] K. Wang, G. Boussinot, C. Hüter, E. A. Brener, and R. Spatschek, Modeling of dendritic growth using quantitative nondiagonal phase field model, *Phys. Rev. Materials* **4**, 033802 (2020).
- [18] A. Sinhababu, A. Bhattacharya, and S. Ayyalasomayajula, An efficient pseudo–spectral based phase field method for dendritic solidification, *Comput. Mater. Sci.* **186**, 109967 (2021).
- [19] R. Borcia, I. D. Borcia, and M. Bestehorn, Drops on an arbitrarily wetting substrate: A phase field description, *Phys. Rev. E* **78**, 066307 (2008).
- [20] D. Jacqmin, Contact–line dynamics of a diffuse fluid interface, *J. Fluid Mech.* **402**, 57 (2000).
- [21] R. Borcia, I. D. Borcia, and M. Bestehorn, Static and dynamic contact angles – A phase field modelling, *Eur. Phys. J. Spec. Top.* **166**, 127 (2009).
- [22] R. Borcia, I. D. Borcia, and M. Bestehorn, Can vibrations control drop motion? *Langmuir* **30**, 14113 (2014).
- [23] R. Borcia, I. D. Borcia, M. Bestehorn, O. Varlamova, K. Hoefner and J. Reif, Drop behavior influenced by the correlation length on noisy surfaces, *Langmuir* **35**, 928 (2019).
- [24] Zhongqian Sun *et al.*, Bubble manipulation driven by alternating current electrowetting: oscillation modes and surface detachment, *Langmuir* **37**, 6898 (2021).
- [25] R. Borcia and M. Bestehorn, Phase–field model for Marangoni convection in liquid–gas systems with a deformable interface, *Phys. Rev. E* **67**, 066307 (2003).
- [26] M. Bestehorn, D. Sharma, R. Borcia, and S. Amiroudine, Faraday instability of binary miscible/immiscible fluids with phase field approach, *Phys. Rev. Fluids* **6**, 064002 (2021).
- [27] V. Jajoo, *Faraday instability in binary mixtures*, Ph.D. thesis, University of Bordeaux, 2017.
- [28] C. Hirsch, *Numerical Computation of Internal and External Flows* (Wiley, New York, 1998), Vol.1, p. 201.
- [29] M. Bestehorn, *Computational Physics* (de Gruyter, Berlin, 2016), p. 121.
- [30] J. H. Ferziger and M. Peric, *Computational Methods for Fluid Dynamics* (Springer-Verlag, Berlin, 2002), p. 167.
- [31] H. Ding, P. D. M. Spelt, and C. Shu, Diffuse interface model for incompressible two–phase flows with large density ratios, *J. Comput. Phys.* **226**, 2078 (2007).
- [32] R. Borcia and M. Bestehorn, A phase field description of self–propulsion of twin sessile drops induced by surface tension gradients, *Fluid Dyn. Res.* **46**, 041405 (2014).
- [33] J. Kou and S. Sun, Thermodynamically consistent modeling and simulation of multi–component flow with partial miscibility, *Comput. Methods Appl. Mech. Eng.* **331**, 623 (2018).
- [34] D. G. A. L. Aarts, H. N. W. Lekkerkerker, H. Guo, G. H. Wegdam, and D. Bonn, Hydrodynamics of Droplet Coalescence, *Phys. Rev. Lett.* **95**, 164503 (2005).
- [35] See Supplemental Material at <http://link.aps.org/supplemental/10.1103/PhysRevFluids.7.064005> for the movie related to Fig. 9.

- [36] R. Borcia, S. Menzel, M. Bestehorn, S. Karpitschka, and H. Riegler, Delayed coalescence of droplets with miscible liquids: Lubrication and phase field theories, [Eur. Phys. J. E \*\*34\*\*, 24 \(2011\)](#).
- [37] S. Karpitschka and H. Riegler, Noncoalescence of Sessile Drops from Different but Miscible Liquids: Hydrodynamic Analysis of the Twin Drop Contour as a Self-Stabilizing Traveling Wave, [Phys. Rev. Lett. \*\*109\*\*, 066103 \(2012\)](#).
- [38] D. Sharma, M. Coquerelle, A. Erriguible, and S. Amiroudine, Adaptive interface thickness based on mobility–Phase field method for incompressible fluids, [Int. J. Multiphase Flow \*\*142\*\*, 103687 \(2021\)](#).

*Correction:* The previously published Figure 8 was missing panel (d) and has been set right.